Measurement 242 (2025) 116018

Contents lists available at ScienceDirect

Measurement

journal homepage: www.elsevier.com/locate/measurement

Automated monitoring of insulation by ultraviolet imaging employing deep learning

Gustavo Aragão Rodrigues [a,*], Bruno Vinicius Silveira Araujo [a], Johnny Herbert Paixão de Oliveira [b], George Victor Rocha Xavier [b], Ulisses Daniel Enes de Souza Lebre [c], Charles Antony Cordeiro [c], Eduardo Oliveira Freire [d], Tarso Vilela Ferreira [b]

[a] Federal University of Campina Grande, INESC P&D Brasil, Brazil
[b] Federal University of Sergipe, INESC P&D Brasil, Brazil
[c] ENEVA S.A, Brazil
[d] Federal University of Sergipe, INESC P&D Brasil, Brazil. Laboratório de Neurociencias y Tecnologias Aplicadas (INSIBIO/CONICET/UNT), Argentina

ARTICLE INFO

Keywords:
UV imaging
Conditional Monitoring
Corona Effect
Computer Vision

ABSTRACT

The corona effect on the surface of electrical system equipment and components generally indicates undesirable phenomena that can lead to physical degradation of materials or even equipment failure. One of the most promising techniques for monitoring corona discharges is the use of specialized cameras for the detection of ultraviolet radiation. This paper introduces an innovative algorithm for classifying the criticality of insulation based on attributes extracted from videos recorded using an ultraviolet detection camera. The attributes extracted from each facula origin include maximum persistence, area, and the minimum distance between the facula origin and the insulation. To obtain this distance, a technique combining a deep convolutional neural network model with an adaptive segmentation thresholding method is proposed. To validate the proposed methodology, inspections were conducted at a 500 kV substation. A total of 96 videos were recorded, within which 99 facula origins were identified. The object detection model applied demonstrated an accuracy of 85.5 % in detecting insulation in images, based on a validation set comprising 1,985 images and 8,730 instances. The results of the classification showed that 72.7 % of the facula origins recorded originated from regions far from the insulation (mainly cables and corona rings). These results demonstrate that the distance between the insulation and the facula origin is an essential attribute for video analysis, providing context for recorded discharges and allowing differentiation between cases where ultraviolet radiation originates from insulation and those where discharge location is less critical.

1. Introduction

In 1838, Michael Faraday published a paper that detailed a series of experiments involving disruptive discharges with various electrodes and polarities. Notably, Faraday reported on a “dark discharge” that preceded the formation of a disruptive light discharge, marking one of the earliest descriptions of the corona effect [1]. Currently, the corona effect is recognized as a nonlinear phenomenon that manifests in regions of intense, non-uniform electric fields. This effect is primarily attributed to the ionization of air and is characterized by partial discharges between the energized conductor and the surrounding air [2].

Within the Electrical Power System (EPS), the corona effect is observed across a range of electrical equipment and voltage levels. The causes of this effect are multifaceted, encompassing sharp metal structures and insulation defects. Corona discharges may lead to several adverse outcomes, including interference in communication systems, power losses, and long-term insulation degradation [3].

Insulation failure can precipitate transmission line shutdowns,

* Corresponding author.
E-mail addresses: gustavo.aragao.rodrigues@ee.ufcg.edu.br (G. Aragão Rodrigues), bruno.vinicius.silveira@ee.ufcg.edu.br (B. Vinicius Silveira Araujo), john3008@academico.ufs.br (J. Herbert Paixão de Oliveira), george.xavier@academico.ufs.br (G. Victor Rocha Xavier), ulisses.lebre@eneva.com.br (U. Daniel Enes de Souza Lebre), charles.cordeiro@eneva.com.br (C. Antony Cordeiro), efreire@academico.ufs.br (E. Oliveira Freire), tarso@academico.ufs.br (T. Vilela Ferreira).

https://doi.org/10.1016/j.measurement.2024.116018
Received 22 July 2024; Received in revised form 15 October 2024; Accepted 16 October 2024
Available online 19 October 2024

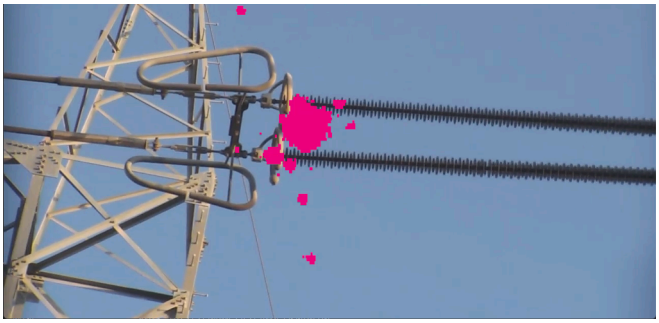

Fig. 1. Manifestation of UV in the form of faculae in magenta color. (For interpretation of the references to color in this figure legend, the reader is referred to the web version of this article.)

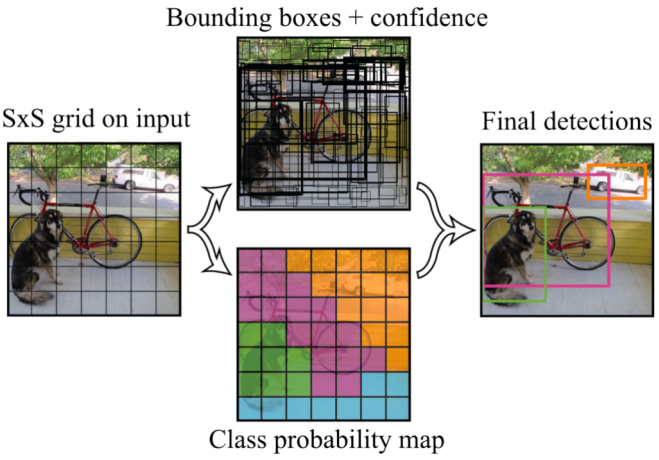

Fig. 2. Operation of YOLO [23].

resulting in discontinuities in electricity supply. Such failures cause operational losses for the utility company, including revenue loss and potential fines imposed by regulatory agencies. Additionally, insulation failure can negatively impact key energy system quality indicators, such as reliability and supply availability. Given these implications, monitoring discharges in substations and transmission lines is of great importance.

A well-established technique for monitoring insulators is the measurement of leakage current, which stands out for its low implementation cost, extensive scientific validation, and suitability for real-time applications [4]. Over the past few years, various studies have been published aiming to diagnose the operating condition of insulators based

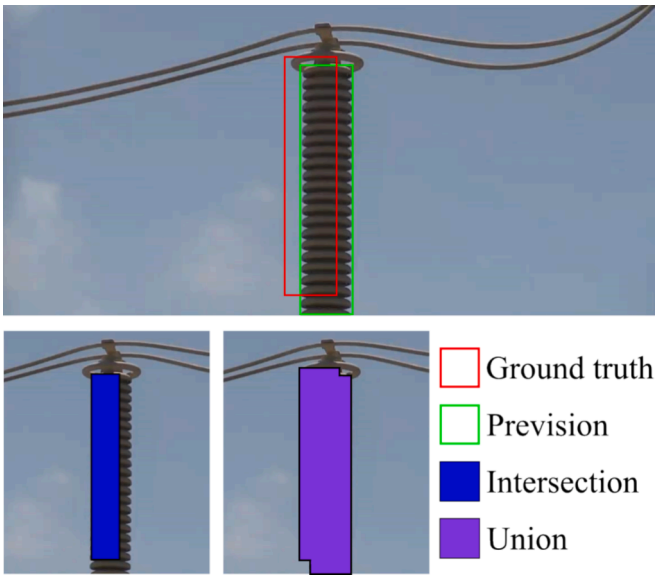

Fig. 4. Illustration of the intersection and union from the ground truth and predicted BBox.

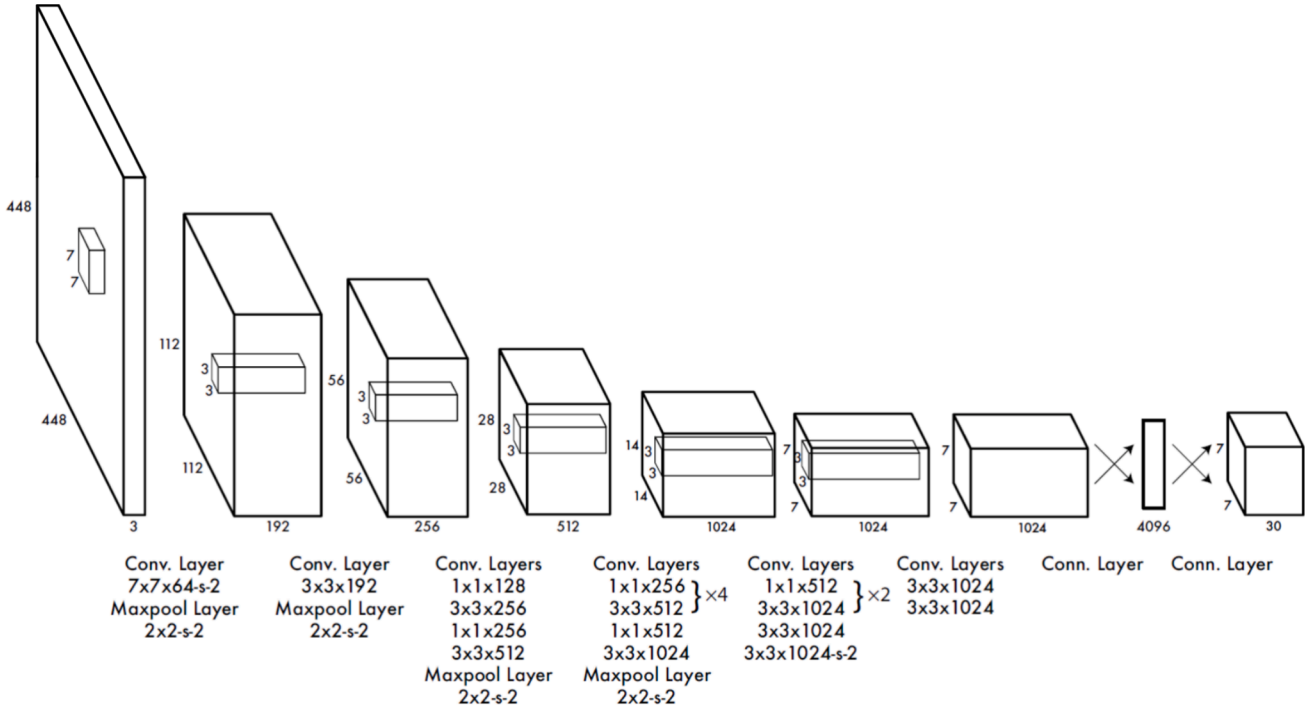

Fig. 3. YOLO CNN model [23].

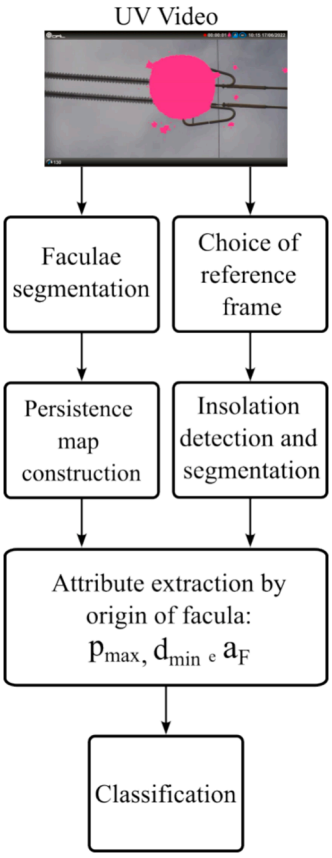

Fig. 5. Flowchart of the methodology.

Table 1
Equipment considered in the research.

Acronym	Equipment	Part detected
DS	Disconnecting switch	Insulating column
CB	Circuit breaker	Insulating column and bushing
SI	Suspension insulator	Polymer
PI	Pedestal insulator	Insulating column
SA	Surge arrester	Insulating column
VT	Voltage transformer	Insulating column
CT	Current transformer	Insulating column
PT	Power transformer	Bushing

on their leakage current measurements.

In [5], an online diagnostic system for ceramic insulators was developed based on their leakage current data. The authors conducted numerous experiments and observed a strong correlation between the ratio of the third and fifth harmonics and critical operating conditions of the insulators. In [6], an extended version of the equivalent circuit model for polluted insulators was proposed. The new model allowed for the experimental estimation of the contamination level of insulators based on their leakage current measurements. In [7], an automated detection device was fabricated for monitoring power distribution lines. The equipment is equipped with a leakage current meter capable of diagnosing the operating condition of the insulators. The prototype was tested in both laboratory and practical applications and demonstrated reliable performance.

Despite being a well-established technique in literature with significant potential, leakage current measurement is not the most suitable for monitoring corona discharges. The effects of these discharges can be observed in the leakage current; however, it is not possible to precisely locate and quantify them. On the other hand, UV imaging monitoring has the capability to quantify and locate corona discharges. Additionally, with modern computer vision techniques, it is possible to differentiate distinct sources of discharges and process them individually. Thus, this technique emerges as the most suitable for monitoring corona effects in power system equipment. During surface or corona discharges, ultraviolet (UV) radiation and visible light are emitted, among other physical manifestations [8]. UV imagers are specifically designed to detect the UV radiation produced by the corona effect, particularly within the 240 to 280 nm range. This range corresponds to the solar UV-C spectrum, which is filtered by the ozone layer and does not reach the lower atmospheric layers. This characteristic allows corona detectors for daytime inspections without interference from solar radiation. The cameras visually represent UV radiation in the form of faculae, as exemplified in Fig. 1. Normally, faculae are represented by the color white, but in modern cameras, this color can be configured by the user. For Computer Vision (CV) applications, it is recommended to choose a color that makes these faculae easily distinguishable from the rest of the image.

Despite the robustness of the technique, the use of such cameras does not guarantee an accurate diagnosis, interpreting facula patterns requires subjective video analysis, which depends on the skill and experience of the inspector. Extracting parameters of interest from the videos generated during inspections is neither straightforward nor automated, and the quantification and localization of the discharges is a challenging task. Due to the relevance of the topic, several studies have been conducted in recent years to improve the accuracy of UV imaging inspections. Most of this research employs Digital Image Processing (DIP) algorithms to extract UV information from images and videos, and thus propose quantification or classification attributes of the detected discharges.

Some research has been carried out with the aim of understanding how measurement characteristics influence the detected UV radiation. In [9], the effect of camera gain and capture distance was analyzed, leading to the development of a model to estimate the magnitude of discharges from the faculae area. Similarly, [10] investigated the effect of gain and capturing distance based on two parameters: average area of faculae per frame and average number of photons per frame. In [11], UV imaging was used to compare the intensity of surface discharges in insulators subjected to different levels of pollution and humidity.

Other authors have concentrated their efforts on classification tasks, be it the operating condition of the insulator, the type of discharge detected, or the level of pollution of the insulators. In these studies, it is common to combine UV imaging with other monitoring techniques to achieve more accurate results. In [12], images from three spectra (visible, infrared, and UV) were used to estimate the level of saline pollution in insulators. As a UV parameter, the maximum facula area between frames was selected. In [13], an algorithm was developed to combine UV imaging data with acoustic emission sensors to detect defective insulators. In [14], a classifier was developed based on the spectrogram of radiation captured by a UV sensor to classify discharges into three types of severity: corona discharge, local arc, and long arc. In [15], an algorithm for classifying the operational condition of porcelain insulators using UV imaging was developed. The proposed classification technique was based on the fuzzy c-means clustering algorithm. However, the method lacks modern computer vision tools that enable the individualization of discharge origins and the use of persistence as a classification attribute. Additionally, the technique was applied to only one real-world case.

These classification works normally present methodologies that are still limited to application in laboratories or controlled environments. For applications in real conditions, a series of challenges and obstacles arise. The main issue affecting UV imaging in substations and transmission lines is the massive presence of corona discharges in the environment and the lack of control over meteorological conditions. These situations require more robust methodologies that differentiate when the detected discharge is or is not correlated with the monitored equipment.

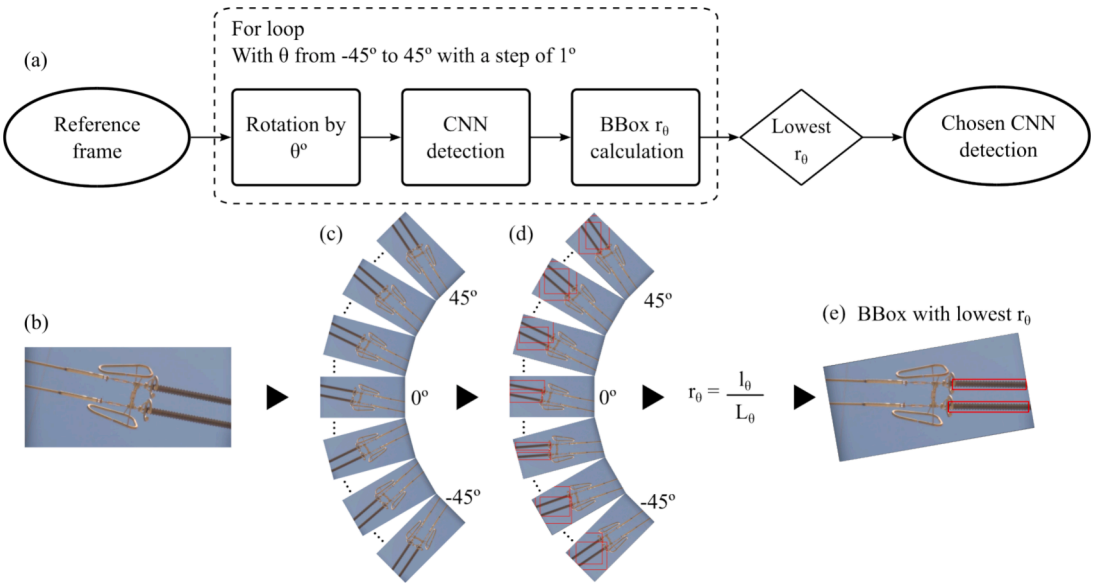

Fig. 6. Detection flowchart. (a) Flowchart of the detection algorithm. (b) Reference frame. (c) Representation of images rotated from −45° to 45°. (d) Insulation detection in all rotated images. (e) Detection with lower value of r_θ.

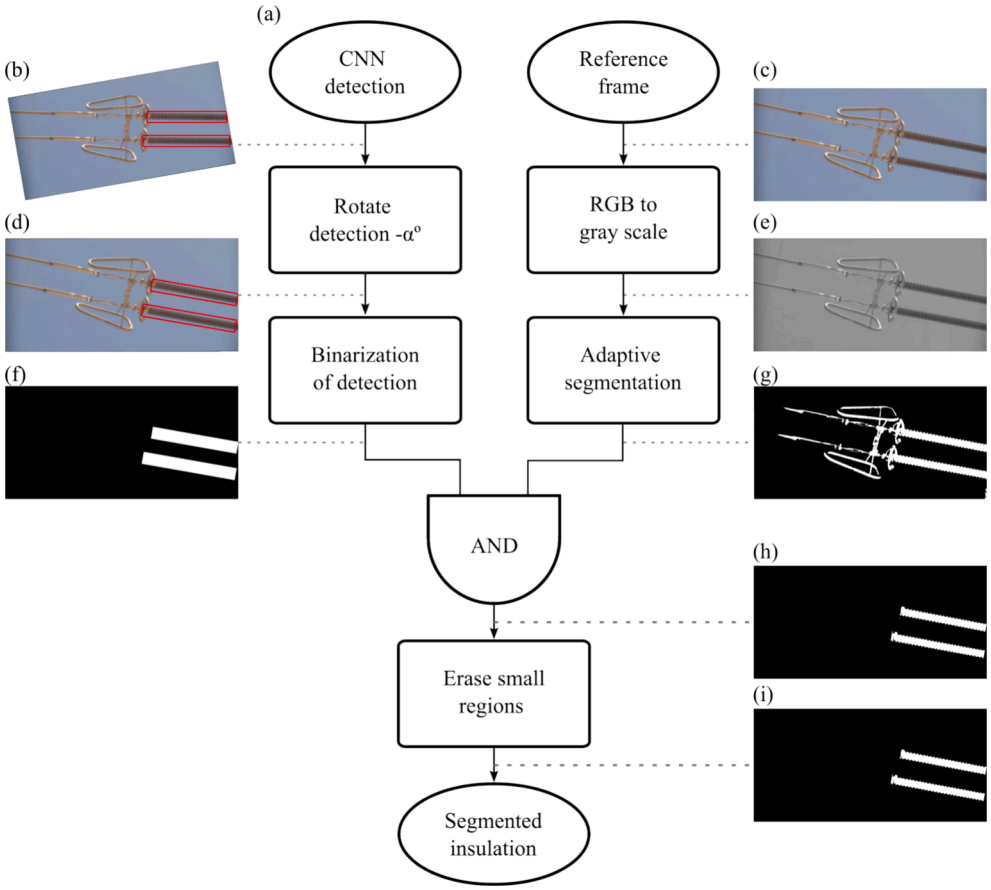

Fig. 7. Segmentation flowchart. (a) Block diagram of the segmentation step. (b) Image resulting from the detection step. (c) Reference frame. (d) Detection rotated back to the original position (−α°). (e) Reference frame converted to grayscale. (f) Binarized image of insulation detection. (g) Binarization by adaptive thresholding of the grayscale reference frame. (h) Result of the AND operation between the binarized detection and the adaptive segmentation result. (i) Binary image of the segmented insulator after small regions are deleted.

Recent studies leveraging modern CV techniques, the aim is not only to quantify the detected UV radiation, but also to contextualize it in relation to the monitored scene. In [16], the applied object detection algorithm YOLOv3 was trained to detect insulation in images of electrical equipment in a power substation. The authors also proposed combining the trained model with UV imaging for the diagnosis of

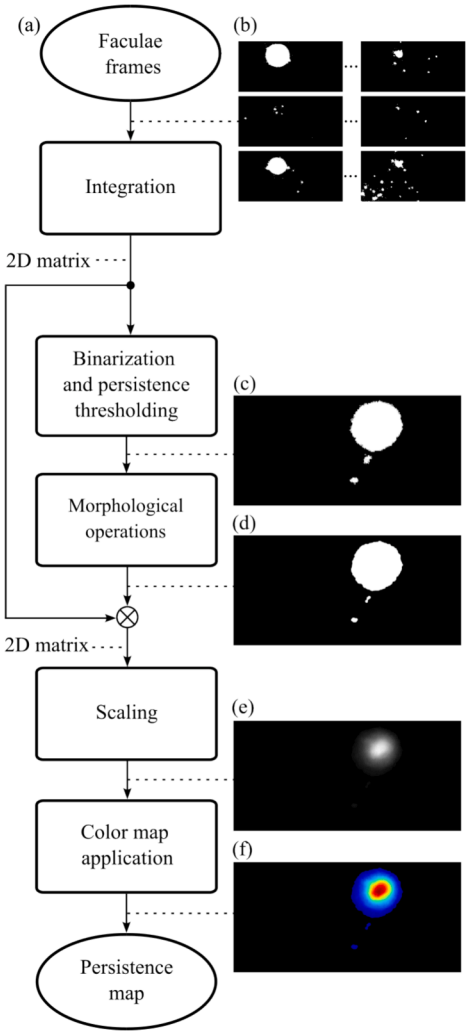

Fig. 8. Flowchart of the persistence map construction steps. (a) Methodological flowchart. (b) Set of binary images that contain the faculae segmentation for each frame of the video. (c) Binarization of the matrix using the persistence threshold. (d) Result of digital morphology operations. (e) Scaling of the result of multiplying the binary persistence map by the matrix resulting from the integration of the facula frames.(f) Result of applying a color map to the previous step.

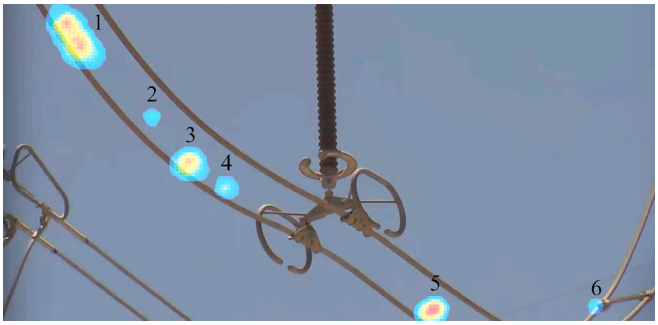

Fig. 9. Facula origin's representation.

insulators. However, a detailed methodology for this purpose was not presented. Similarly, in [17], the Faster R-Convolutional Neural Network (CNN) was applied to detect distribution voltage equipment in UV video, and the criticality of the equipment was classified based on the ratio between the UV manifestation area and the network detection

Table 2
Results from YOLOv5 training.

Images	Instances	*p*	*r*	mAP50	mAP50-95
1985	8730	0.855	0.817	0.888	0.556

Bounding Box (BBox). Despite offering an important contribution to research in UV imaging, the authors limited the analysis of UV information to a few frames of the video, and consequently, the persistence of the discharges was not used in the classification. Furthermore, the proposed classification method can be improved by adding new attributes and considering the location of the discharge origins. In [18], a methodology for the extraction of relevant parameters from UV videos was introduced, which made it possible to understand how these parameters are influenced by different insulation conditions. The authors demonstrated that the proposed summary could simplify the diagnosis of the equipment's operating condition. However, the extracted parameters may not be the most suitable for evaluating the criticality of the discharges, since the area and perimeters are strongly correlated, and the shape factor can hardly be associated with the severity of the discharge.

Building on the concept of contextualizing detected corona discharges, a methodology was developed in [19] to classify corona discharges detected by a UV camera in polymeric insulators (500 kV). In addition to utilizing the persistence map previously introduced by other researchers, the referenced work proposed a novel attribute for classification: the distance between the discharge sources and the insulator. To achieve this, the insulator was segmented in the images using the Otsu method in the blue channel. However, as noted in [14], the segmentation method presented is not sufficiently robust and, despite its application to practical conditions, it still needs improvements.

This paper presents an innovative methodology based on the DIP and CV algorithms for the automated extraction of features from UV images and the subsequent estimation of the criticality of the monitored insulation. The proposed algorithm initially integrates the UV information detected by the camera into a persistence map. Regions are subsequently delineated on this map, understood as distinct "facula origins". The following parameters are extracted from each of these regions: maximum persistence as a percentage, facula area in square centimeters, and distance to insulation centimeters. A deep CNN model was employed to detect insulations in the images, and an adaptive thresholding method was used to segment them. This approach is innovative and has not been applied before.

From the extracted attributes, each corona source from each video was classified into five distinct cases:

- Case 1: No significant record of corona discharge.
- Case 2: Corona discharge was recorded, but its location was not sufficiently close to the insulation.
- Case 3: Corona discharge was recorded near the insulation, with mild intensity.
- Case 4: Corona discharge was recorded near the insulation, with moderate intensity.
- Case 5: Corona discharge was recorded near the insulation, with high intensity.

The technique presented in this paper is innovative as it separates UV information from the video into different discharge sources based on their position. Consequently, the criticality of the discharge sources is classified by considering their position relative to the inspected insulation. This approach reduces the subjectivity of video analysis by automating this process computationally.

In the following section, some fundamental concepts are presented, essential for understanding this research. Subsequently, in the "Methodology" section, the research methodology is detailed, including a comprehensive description of the developed algorithm. In the "Results"

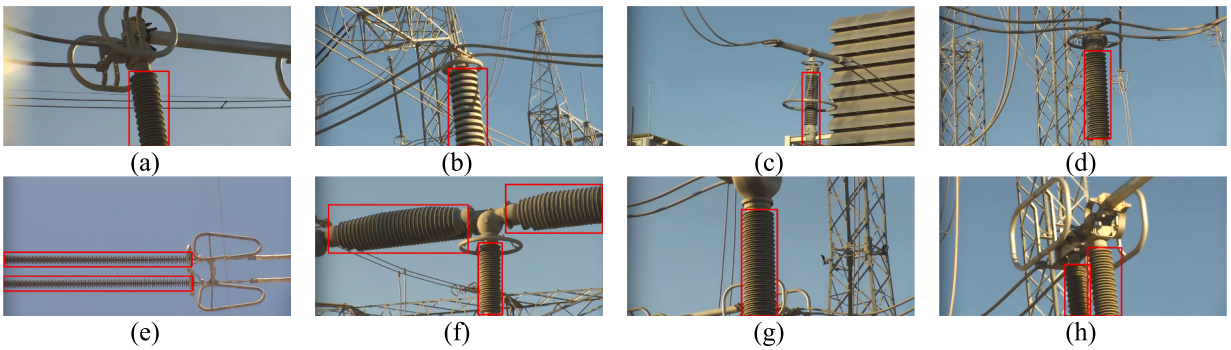

Fig. 10. Examples of insulation detection: (a) Fixed contact of the DS. (c) PI. (e) SA. (g) VT. (e) SI. (f) CB. (g) CT. (h) Movable contact of the DS.

section, the research findings are presented, including the performance of the trained detection model and the validation of the algorithm through substation inspections using a UV camera. Finally, in "Conclusion", the research findings are highlighted, along with prospects for future work.

2. Digital image processing and computer vision algorithms

This section presents the primary DIP and CV algorithms utilized in this research. It includes a description of the principlesof mathematical morphology and the adaptive mean threshold. Additionally, it explains the working principle of YOLO (You Only Look Once), the deep CNN model applied for object detection.

2.1. Mathematical morphology

Mathematical morphology, using a set defined as a structuring element, transforms an image to extract information related to its geometry and topology. The two basic operations of morphology are erosion and dilation [20]. In brief, it can be said that erosion shrinks an image, while dilation expands it. Given the sets A and B defined in a two-dimensional space Z^2 whose components are $a = (a_1, a_2)$ and $b = (b_1, b_2)$, to perform the operation of dilation of A by B is to obtain the set of displacements x for which the intersection of $(\widehat{B})_x$ and A includes at least one element other than 0. Let $\widehat{B}$ be the reflection of B, obtained by [20]:

$$\widehat{B} = \{x | x = -b, for\, b \in B\}, \tag{1}$$

and let $(B)_x$ be the translation of B for $x = (x_1, x_2)$, defined by:

$$(B)_x = \{c | c = b + x, for\, b \in B\}. \tag{2}$$

Thus, the dilation operation, denoted by $A \oplus B$, can be defined as:

$$A \oplus B = \left\{x \middle| \left[(\widehat{B})_x \cap A\right] \subseteq A\right\}. \tag{3}$$

The erosion operation, in turn, results in the set of points x such that B, translated from x, is contained in A. In mathematical terms, erosion ($A \ominus B$) is obtained by:

$$A \ominus B = \{x | (B)_x \subseteq A\}. \tag{4}$$

The combination of erosion and dilation (with a reflected structuring element) results in two additional operations: closing and opening. The closing operation, which involves dilation followed by an erosion and tends to fuse small breaks, widen narrow gaps, eliminate holes, and fill empty spaces in the contour. Conversely, opening, which consists of an erosion followed by a dilation, softens contours, breaks narrow regions, and removes slender protrusions [21].

2.2. Adaptive thresholding

Thresholding is the process that determines the threshold (T) for the binarization of image pixels, effectively converting a grayscale image into a binary (black-and-white) image. Traditionally, global threshold methods, such as Otsu's method, are employed to compute a single T value for the entire image. However, these global methods often underperform when the image exhibits a significant variety of pixel intensity due to lighting changes or complex shapes [22].

Adaptive thresholding methods minimize this problem by calculating T for each pixel in the image according to statistical criteria related to the pixel's neighborhood. Several statistical approaches can be used, such as the arithmetic mean of this neighborhood, which can be calculated by [22]:

$$T = mean(I_L) - C \tag{5}$$

where I_L is a region of the image and C is a constant used for fine-tuning the segmentation. The size of the region, I_L can also be adjusted, and different sizes of this region tend to vary the segmentation performance significantly. Thus, it is crucial to define the optimal window size for each application.

2.3. You only Look Once (YOLO)

YOLO is an object detection algorithm based on deep neural networks and was originally published in 2015 [23]. It is a methodology that unifies different aspects of object detection into a single CNN so that the network uses the characteristics of the entire image to predict each BBox. By predicting all BBoxes simultaneously, YOLO facilitates real-time inferences with high average accuracy. A summary of the algorithm's functioning can be seen in Fig. 2.

The YOLO algorithm operates in three main steps: resizing the image, applying the CNN to the image, and determining the accepted detections based on the model's confidence scores. Initially, the image is divided into a mesh of $S \times S$ cells, in which each cell predicts the number of BBoxes B and the reliability factor for only one class. The initial convolutional layers extract the characteristics of the image, while the fully connected layers predict the probability and coordinates of the output BBox. The first 24 layers of the model are convolutional, while the last two are completely connected layers. The full architecture of the YOLO model can be seen in Fig. 3.

2.3.1. Metrics for evaluating YOLO performance

Object detection algorithms usually make their predictions through BBoxes, which the region containing the object of interest. In the training process, a parameter is needed to verify that the predicted BBox aligns to the labeled one. Therefore, the Intersection over Union (IoU) is used, which can be calculated by the following equation [24]:

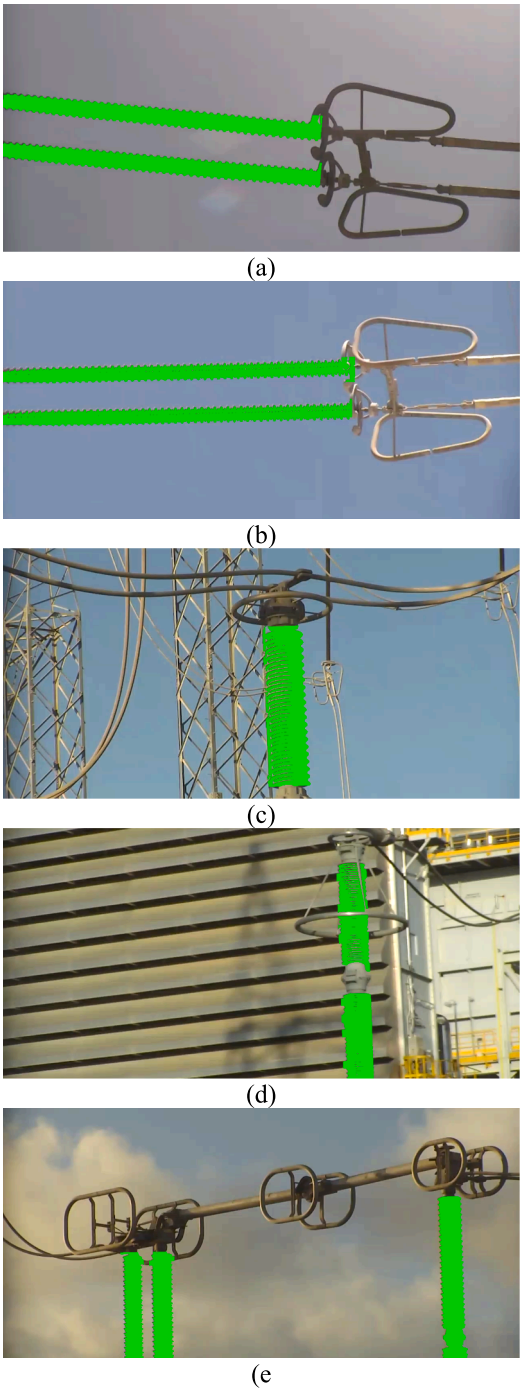

Fig. 11. Examples of segmentation. (a) Polymer of an IS. (b) Polymer of an IS. (c) Insulating column of a PT. (d) Insulating column of an SA. (e) Insulating columns of a DS.

$$IoU = \frac{intersection\ area}{union\ area}. \tag{6}$$

In Fig. 4 it is illustrated the practical significance of the intersection area and the union area. An IoU of 0.5 indicates that the prediction will only be considered correct if the calculated IoU is equal to or greater than 0.5.

In general, the performance of an object detection algorithm is evaluated in terms of precision (p), recall (r), and Mean Average Precision (mAP). Precision quantifies the percentage of correct predictions and can be calculated by:

$$p = \frac{TP}{TP + FP}, \tag{7}$$

where TP is the number of true positives, while FP is the number of false positives. The recall quantifies the percentage of TP found.

$$r = \frac{TP}{TP + FN}, \tag{8}$$

where FN is the number of false negatives. The mAP is calculated from the area under the curve of the precision × recall chart, which can be calculated by:

$$AP = \int_0^1 p(r)dr, \tag{9}$$

The mAP50 then considers an IoU of 0.5, while the mAP50:95 considers an average result of the IoU variation from 0.5 to 0.95, with steps of 0.05.

3. Methodology

The proposed methodology uses the DIP and CV techniques to extract parameters from UV videos for the automatic classification of the insulation condition. In Fig. 5 a flowchart of the proposed methodology is presented.

Faculae are extracted from the UV video frame-by-frame, resulting in a series of binary matrices that contain only UV information. These - frames are processed to generate a persistence map, in which a single image summarizes the behavior of the faculae throughout the entire video. In parallel, a reference frame is chosen and used for the detection and segmentation of insulations. Finally, the criticality classification of each facula origin recorded in the video is performed. In this paper, a facula origin refers to a region on the persistence map with a persistence greater than 2 % of the frames in the video.

The algorithm was developed to be fast and computationally efficient. To achieve this, vectorized operations and logical operations were adopted, which are generally faster than scanning the matrices that constitute the images. Additionally, binary images were used whenever possible, significantly reducing RAM usage.

The 96 videos used in this research were recorded by a DayCor Luminar HD camera, each approximately 30 s long (around 720 frames each, 72,000 frames in total). The recordings took place in a 500 kV substation belonging to the Port of Sergipe I Thermoelectric Power Plant, owned by ENEVA S.A., in the city of Barra dos Coqueiros, Brazil.

3.1. Faculae extraction

As illustrated in Fig. 1, the camera is configured to display the faculae in magenta, allowing for their extraction using color thresholds. The thresholds applied were:

- $R \geq 200$
- $G \leq 100$
- $130 \leq B \leq 160$

This process yields the facula matrices (F_j), which are binary matrices in which the facula pixels are taken as 1 and the non-facula pixels as 0, and j represents the frame of the video. This procedure is repeated for eachframe, and each matrix F_j is saved by composing a set of binary matrices that contains only the UV information of the original video. The reference frame (img_{ref}) is a video frame that contains the smallest number of faculae (typically zero).

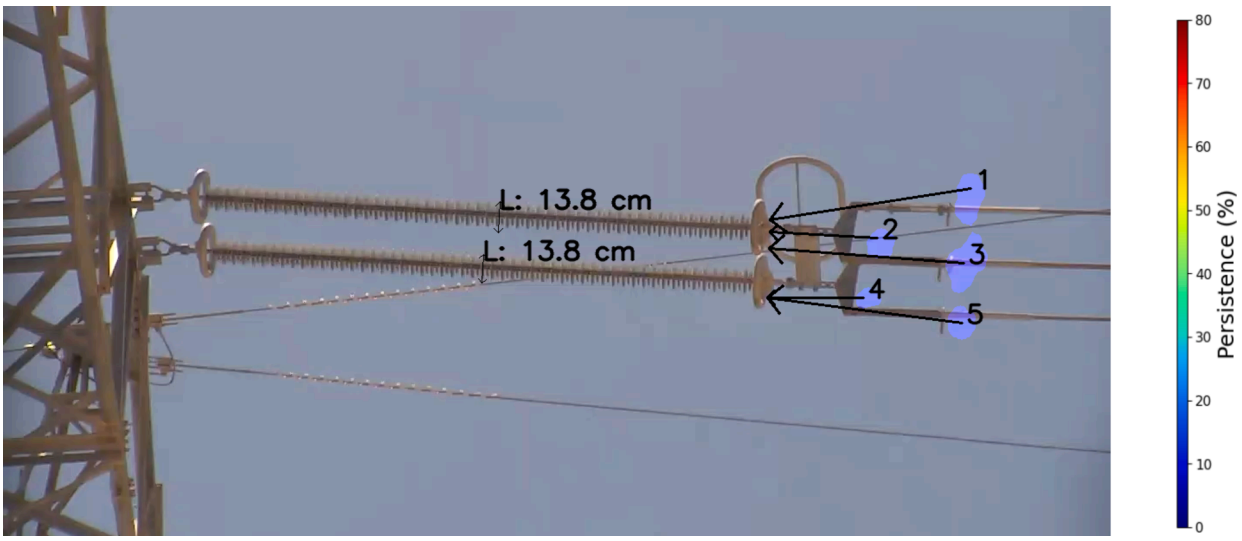

Fig. 12. First examples of application of the proposed algorithm.

Table 3
Numerical results of Fig. 12 by discharge origin (n°).

n°	x	y	P_{max}[%]	a_F[cm^2]	d_{min}[cm]	Class
1	0.87	0.34	6.43	219.1	88.5	2
2	0.79	0.43	4.46	125.5	46.8	2
3	0.87	0.48	9.19	292.7	85.0	2
4	0.78	0.54	3.54	90.7	46.0	2
5	0.87	0.59	8.01	168.2	94.1	2

3.2. YOLOv5 training

In this research, YOLOv5[1] was used to detect the insulation of electrical equipment. Table 1 shows the equipment considered and the parts detected by the model as a single generalized label.

The image database used for model training comprised of 3,329 digital camera images, 2,839 thermography images, and 452 UV camera video frames, totaling 6,620 images. This dataset includes images captured at various times of the day, including nighttime, under

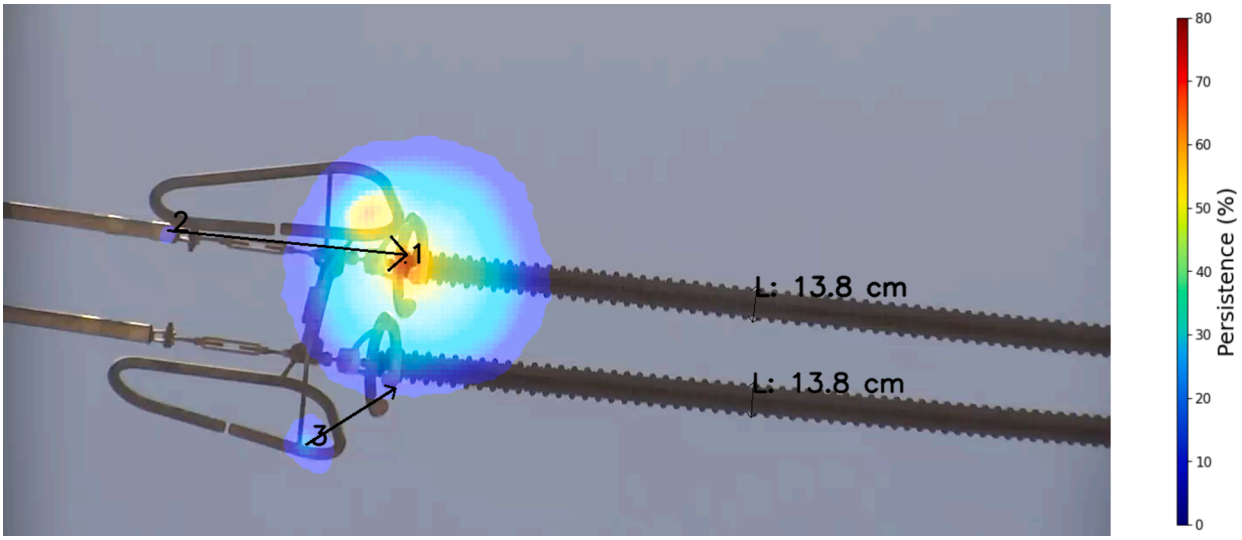

Fig. 13. Second example of application of the proposed algorithm.

Table 4
Numerical results of Fig. 13 by discharge origin (n°).

n°	x	y	P_{max}[%]	a_F[cm^2]	d_{min}[cm]	Class
1	0.36	0.48	65.6	7881.0	0	5
2	0.15	0.42	3.4	33.9	90.2	2
3	0.27	0.82	19.5	317.7	40.6	2

different lighting and background conditions. This dataset was randomly divided into a 70/30 ratio for training and validation.

To artificially expand the training set, each of the 4,635 images was rotated at angles of 60°, 120°, 180°, 240°, and 300°, generating five new images per original image. Subsequently, a copy of each image is created, and one of the following color transformations is randomly applied to these copies: binarization, conversion to grayscale,

[1] YOLOv5s is the fifth version of YOLO developed by the Ultralytics LLC team and is a smaller model that boasts high recognition speed [25].

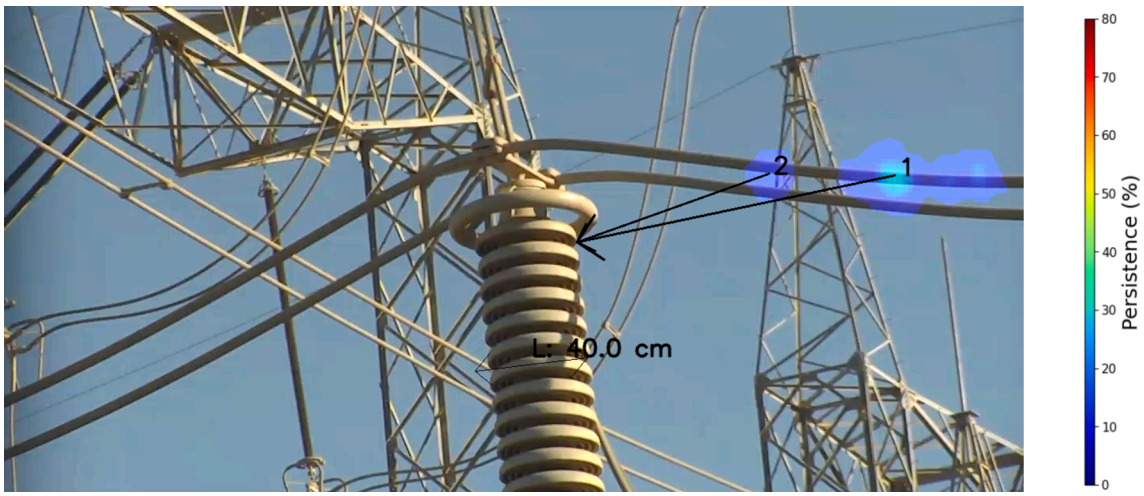

Fig. 14. Third example of application of the proposed algorithm.

Table 5
Numerical results of Fig. 14 by discharge origin (n°).

n°	x	y	P_{max}[%]	a_F[cm^2]	d_{min}[cm]	Class
1	0.87	0.34	29.58	1066.6	114.6	2
2	0.75	0.34	11.41	261.8	71.9	2

Table 6
General classification result.

Day	Relative humidity (%)	No. Videos	No. Origins of Facula	Classification Case 1	Case 2	Case 3	Case 4	Case 5
1	66.8	25	46	6	**37**	5	3	1
2	70.9	38	39	16	**23**	8	7	1
3	69.1	24	11	**16**	10	0	1	0
4	61.2	9	3	**7**	2	0	0	1

conversion to HSV, conversion to YUV, exclusion of the red channel, exclusion of the green channel, and exclusion of the blue channel.

In this way, a dataset comprising 48,800 images for training and 1,985 for validation was obtained, resulting in a total data size of 6.12 GB. The YOLOv5 model, pre-trained on the COCO[2] dataset, was subsequently fine-tuned using the expanded dataset for up to 300 epochs. This training was conducted locally on a notebook with an Intel(R) 12th Gen Core (TM) i7-12650H processor (2.70 GHz), 16 GB RAM, and an NVIDIA GeForce RTX 3070 Ti graphics card (8 GB).

3.3. Insulation detection

The segmentation of the insulation in the image is divided into two steps. The block diagram shown in Fig. 6 illustrates the algorithm of the first step.

First, the img_{ref} is rotated 90 times at angles ranging from -45° to 45°; for each case, inference is made with the YOLOv5 model, as seen in Fig. 6c and 6d. Then, the angle at which the ratio (r_θ) between the smallest side (l_θ) and largest side (L_θ) of the BBox is at its minimum is selected. The goal of this step is to find the ideal rotation angle (α) that leaves the insulation in the most horizontal or vertical position (Fig. 6e).

[2] The Microsoft COCO (Common Objects in Context) image database has 328,000 images with a total of 2.5 million labeled instances in 91 different classes. Classes are common everyday objects and animals in a typical context. This database is widely used in object detection and segmentation research [26].

This is advantageous because the YOLOv5 BBox has only straight vertical/horizontal lines; that is, detecting inclined insulation is disadvantageous, since the BBox starts to occupy an unnecessarily large area, which increases the incidence of errors in the segmentation step.

3.4. Insulation segmentation

Fig. 7 shows a flowchart of the segmentation step. In this step, img_{ref} rotated at the angle selected by the previous step goes through the adaptive thresholding of the mean [22]. The results of this operation are multiplied by the result of detection with YOLOv5, which results in the image of the segmented insulation (Img_{seg}). To correct possible problems, binarization correction is applied, which performs a NOT operation if the previous result is reversed (white background and black insulation). Finally, the morphological opening operation is applied, and then all small regions are erased from Img_{seg}.

3.5. Persistence map

The persistence map is built from an integration process that aggregates all the information from the video into a single image, providing relevant information about the detected UV. This allows for the summarization of features scattered throughout the video into a single visual result. Fig. 8 illustrates a block diagram of the persistence map construction algorithm. In Fig. 9, an example of a persistence map with 6 distinct facula origins can be seen.

The first step is to obtain the persistence matrix (P_{map}) by summing the matrices F_j according to the equation:

$$P_{map} = \sum_{j=1}^{N_{frames}} F_j \,, \tag{10}$$

where N_{frames} is the total number of frames in the video. The next step is to apply a threshold to eliminate regions with very low persistence,

which are therefore not relevant. For this, the Boolean matrix (P_{bool}) is constructed, which has a value of 1 for every pixel of the same index in P_{map} greater than 2 % of the value of N_{frames}; the resulting binary image appears in Fig. 8d.

Then, P_{bool} goes through two morphological operations in sequence, opening and closing, with the structuring element with disc format and 15 × 15 pixels dimension. Finally, P_{map} is multiplied by P_{bool} pixel by pixel, resulting in a matrix in which the discharge sources are separated from each other and better highlighted (Fig. 8e). For visualization purposes, this matrix is scaled from 0 to N_{frames} to 0 to 255 and a color map is applied to facilitate the interpretation of the results, giving rise to the image of the persistence map $\left(img_{map}\right)$, as can be seen in Fig. 8f.

3.6. Features extraction

From the UV video and based on the different corona discharge origins highlighted in Im_{map}, the following parameters are extracted by k origin: maximum persistence (p_{max}), facula area (a_F), and the minimum distance between the sources of faculae and the insulation (d_{min}).

To calculate d_{min}, the regions in the matrix Im_{map} are located by 8-neighborhood. Each of these k regions are interpreted as coming from a different source of corona discharge. Thus, the indexing (x_k, y_k) of the pixel with the greatest persistence in each region is obtained. Then, the distance $(d_{k,r})$ between (x_k, y_k) and any pixel (r) of the segmented insulation is calculated by the Euclidean distance equation as follows:

$$d_{k,r} = \sqrt{(x_r - x_k)^2 + (y_r - y_k)^2}, \tag{11}$$

where (x_r, y_r) are the coordinates of any pixel in Im_{seg} which is part of segmented insulation. That way, the value of d_{min} is the smallest value of $d_{k,r}$ obtained by applying equation (11) for all pixels equal to 1 in Im_{seg}. As there may be multiple facula origins in the persistence map, this procedure must be repeated for each of them.

The p_{max} value per facula origin k is equal to the maximum value of the corresponding region in Im_{map} and can be obtained as a percentage by applying:

$$p_{max}\,[\%] = p_{max}\frac{100}{N_{frames}}\,. \tag{12}$$

Given that the width of the insulation for each piece of equipment is known, it is possible to calculate the width (in pixels) of the insulation closest to a facula origin. Then, to facilitate the interpretation of the results, the d_{min} value is converted to centimeters by applying the following equation:

$$d_{min} = d_{pixel}\frac{w_{cm}}{w_{pixel}}\,, \tag{13}$$

where d_{pixel} is the distance from facula origin to the insulation in pixels, w_{pixel} is the width of the insulation in pixels and w_{cm} is the width of this insulation in centimeters. Similarly, a_F is converted to square centimeters. This is done by squaring the width of the insulation in both centimeters and pixels, and calculating the ratio as follows:

$$a_F = a_{pixel}\frac{{w_{cm}}^2}{{w_{pixel}}^2}\,, \tag{14}$$

where a_{pixel} is the number of pixels in a facula origin. This conversion mitigates the influence of the video capture distance on the classification result, as the amplitude of UV radiation recorded is inversely proportional to the square of the distance between the generating source and the observer.

3.7. Classification

This paper employsthe classification method published in [19], which is based on characteristics extracted from the video. For each of the three parameters, three ranges of values (0, 1, and 2) were established, and a table was proposed that relates each combination of ranges to a classification. The ranges established for each parameter are:

$$\mathrm{P} = \begin{cases} 0, if\, \mathrm{p_{max}} < 2\% \\ 1, if\, 2\% \le \mathrm{p_{max}} < 30\% \\ 2, if\, \mathrm{p_{max}} \ge 30\% \end{cases} \tag{15}$$

$$\mathrm{A} = \begin{cases} 0, if\, \mathrm{a_F} < 150\mathrm{cm}^2 \\ 1, if\, 150\mathrm{cm}^2 \le \mathrm{a_F} < 2000\mathrm{cm}^2 \\ 2, if\, \mathrm{a_F} \ge 2000\mathrm{cm}^2 \end{cases} \tag{16}$$

$$\mathrm{D} = \begin{cases} 0, if\, \mathrm{d_{min}} > 25cm \\ 1, if\, 25cm \ge \mathrm{d_{min}} > 10cm \\ 2, if\, \mathrm{d_{min}} \le 10cm \end{cases} \tag{17}$$

Case 1 differs from the others as it is a classification for the entire video, while the other cases relate specifically to a facula origin present in the video. The following equations and inequalities define the classification based on the values of P, A and D.

Case 1.

$$P = 0 \,\text{and}\, A = 0, \tag{18}$$

Case 2.

$$D = 0, \tag{19}$$

Case 3.

$$\begin{aligned} &D = 1 \,\text{and}\, P + A < 3, \\ &\text{or} \\ &D = 1 \,\text{and}\, P + A \ge 3 \end{aligned} \tag{20}$$

Case 4.

$$D = 2 \,\text{and}\, P + A < 2, \tag{21}$$

Case 5.

$$D = 2 \,\text{and}\, P + A \ge 2, \tag{22}$$

4. Results

This section presents the results obtained by the research. Initially, the performance of detection and segmentation algorithms is discussed, followed by the performance of the classifier itself.

4.1. Detection with YOLO

The CNN model was configured for 300 epochs of training with the expanded dataset of 48,800 images. The training, however, was automatically interrupted at epoch 160, after the algorithm experienced 100 epochs without improvement in results. Therefore, the best result was obtained at epoch 60, approximately 6 h after the start of training.

Table 2 shows the validation results of the YOLOv5 model. The network was able to detect 85.5 % of TP, and 81.7 % of its predictions were correct. For an IoU of 0.5, mAP was 88.8 %, while for an IoU ranging from 0.5 to 0.95, mAP was 55.6 %. This indicates that the network not only detects correctly but also positions the BBox in a manner very similar to the labeling.

It is noteworthy that the validation dataset, in addition to being large (1985 images and 8730 instances), is also quite heterogeneous, with images from all substation equipment captured with different devices under varying lighting conditions. While it would be possible to achieve superior detection results using a more homogeneous base, it is more advantageous for the model to be a generalist. In other words, increasing

the training and validation dataset can numerically worsen the results but simultaneously improve detection in practical conditions.

In Fig. 10, some inference examples of the YOLOv5 model can be seen. The network was able to generalize the different types of insulation and detect them correctly.

4.2. Segmentation

Fig. 11 shows examples of the application of the proposed segmentation method. The algorithm was able to detect and segment the insulation in the images. As in some cases, the corona ring overlaps the insulator, part of this ring ends up being segmented together. This overlap may introduce minorerrors in d_{min} estimation, representing a limitation of the proposed algorithm. Additionally, holes observed in the internal part of the segmentation do not significantly affect the d_{min} calculation, as the critical factor is the accurate location of the insulator edges.

4.3. Classification

The characteristics extracted from the videos are presented in the form of a table containing the location (x, y) of the facula origins and their respective p_{max}, a_F, and d_{min}. Fig. 12 provides an example of the algorithm's application to a video of an SI, with the width of the polymer marked by the letter L. The algorithm detected five facula origins on the phase side of the insulator. The d_{min} value calculated for each of the origins was between 46.8 and 94.1 cm, which is sufficiently far from the insulator's polymer; therefore, all five of these origins are classified as **Case 2**.

An analysis of Fig. 12 and Table 3 corroborates the algorithm's classification, the discharges appear to come from sharp regions of the hardware and do not pose a significant risk of equipment degradation. In this example, the values of p_{max} and a_F are not relevant, as the algorithm's classification decision was based only on d_{min}, according to equation (17), which implies $D = 0$ for distances greater than 25 cm.

Fig. 13 and Table 4 shows a case in which the algorithm detected three facula origins, two of them were classified as **Case 2** due to their distance from the polymer. One origin was located at the connection of the cable with the insulator hardware, and the other at the corona ring, so neither of which is concerning the equipment's operational condition. However, in this example, there is a facula origin considered relevant: origin number 1 has a low value of d_{min} and high values of p_{max} and a_F, respectively 0 cm, 65.6 %, and 7,871 cm^2. According to equations (15), (16), and (17), the values of P, A, and D were all equal to 2, which results in the classification as **Case 5**.

As a last example, the result of applying the algorithm to a video of a PI can be seen in Fig. 14 and Table 5. Discharges were detected originating in the cable, which did not pose a risk to the PI's polymer coating. The main highlight of this result is the algorithm's ability to calculate d_{min} correctly even for such a complex image with so many elements in the scene background. This accuracy is evidenced by the arrows pointing precisely to the point closest to the insulation.

Table 6 shows the classification results of 96 videos. Of these, 27 did not exhibita significant amount of discharge and were classified as Case 1. In the remaining 61 videos, 144 distinct sources of discharge were detected.

It is noteworthy that many classifications fell under Case 2, indicating that, under practical conditions, many detected discharges are not close to insulation and, consequently, are not of concern in the context of this research. These discharges typically originate from equalizer rings and cables, which do not suffer significant consequences from corona discharges.

Therefore, the importance of using the d_{min} parameter is emphasized in this type of study, as it is crucial to know the origin of the discharge and not just its intensity. Regarding the intensity of the discharges, the attributes p_{max} and a_F appear to best contribute to this quantification.

5. Conclusion

This paper presents an automated and innovative methodology for processing UV camera images applied to the monitoring of corona discharges. The classification parameters, namely p_{max}, a_F, d_{min}, quantify the persistence of captured UV radiation over time, its intensity, and the distance between the discharge origin and the nearest insulation, respectively. These parameters were employed to classify each discharge source into one of five categories. Two of these categories pertain to cases where the discharges do not pose a risk to insulation, while the remaining three differentiate the level of risk to which the equipment is exposed.

A CNN designed for object detection was trained using a database of 6,620 images, which was artificially expanded to 48,800. In the validation phase, with 8,730 instances, the model achieved a precision of 85.5 % and a recall of 81.7 %. Moreover, an automated methodology was employed to segment the insulation; this was done by combining the detection made by the model with the adaptive mean thresholding method. The results demonstrated that the proposed detection and segmentation method is an effective and yields reliable approach.

The classification algorithm was applied to 96 videos recorded with a DayCor Luminar HD at a 500 kV substation. The results showed that the proposed methodology can differentiate the origins of facula and correctly classify their relevance. It became evident that, in field inspections, the d_{min} parameter is significant, as it introduces context to the recorded discharge and allows for the differentiation of discharges whose origin is insulation from those that originate in cables and equalizer rings, among other structures. According to Table 6, in the IS inspections conducted on days 1 and 2, 70.6 % of the detected faculae sources were far from the insulation.

To further enhance the algorithm, it is suggested to develop a semantic object segmentation model that focuses not only on the segmentation of insulation but also on other relevant objects, such as corona rings, cables, gantry structures, tower structures, etc. This approach will enable the addition of even more context to the classification of discharges and lead to a more assertive diagnosis. Furthermore, the classification algorithm is suitable for real-time applications, and efforts should be made to incorporate it into a continuous monitoring system.

CRediT authorship contribution statement

Gustavo Aragão Rodrigues: Writing – review & editing, Writing – original draft, Visualization, Validation, Software, Methodology, Investigation, Formal analysis, Data curation, Conceptualization. **Bruno Vinicius Silveira Araujo:** Writing – review & editing, Software, Investigation, Formal analysis. **Johnny Herbert Paixão de Oliveira:** Software. **George Victor Rocha Xavier:** Writing – review & editing, Supervision, Formal analysis. **Ulisses Daniel Enes de Souza Lebre:** Project administration. **Charles Antony Cordeiro:** Project administration. **Eduardo Oliveira Freire:** Writing – review & editing, Supervision, Formal analysis, Conceptualization. **Tarso Vilela Ferreira:** Writing – review & editing, Writing – original draft, Supervision, Project administration, Methodology, Investigation, Formal analysis, Conceptualization.

Declaration of competing interest

The authors declare that they have no known competing financial interests or personal relationships that could have appeared to influence the work reported in this paper.

Acknowledgements

This work was developed as part of the project GImpSI - *Gestão dos Impactos da Salinidade em Isolamentos* with ENEVA S.A. and INESC P&D Brasil, under the framework of the R&D Program of the National Agency of Electric Energy (ANEEL), code PD-11278-0001-2021. This work was supported in part by the Coordination for the Improvement of Higher-Level Personnel (CAPES) – Finance Code 001.

Data availability

The authors do not have permission to share data.

References

[1] M. Faraday, Experimental Research in Electricity – thirteenth series, Philosophical Transactions of the Royal Society of London (1838).
[2] P.A. Laplante, Electrical Engineering Dictionary; CRC Press LLC: Boca Raton, FL, USA, 2000.
[3] E. Kuffel, W.S. Zaengl, J. Kuffel, High Voltage Engineering, 2rd ed., Newnes, Oxford, 2000.
[4] R. Ahmed, T. Kim, Y.J. Lee, et al., Online Condition Monitoring and Leakage Current Effect Based on Local Area Environment, Trans. Electr. Electron. Mater. 21 (2020) 144–149, https://doi.org/10.1007/s42341-020-00184-1.
[5] M.F. Palangar, M. Mirzaie, Detection of Critical Conditions in Ceramic Insulators Based on Harmonic Analysis of Leakage Current, Electric Power Components and Systems 44 (16) (2016) 1854–1864, https://doi.org/10.1080/15325008.2016.1183723.
[6] M. F. Palangar, M. Mirzaie and A. Mahmoudi, Improved flashover mathematical model of polluted insulators: A dynamic analysis of the electric arc parameters, Electric Power Systems Research, Volume 179, 2020, 106083, ISSN 0378-7796, Doi: 10.1016/j.epsr.2019.106083.
[7] M.F. Palangar, S. Mohseni, M. Mirzaie, A. Mahmoudi, Designing an Automatic Detector Device to Diagnose Insulator State on Overhead Distribution Lines, IEEE Transactions on Industrial Informatics 18 (2) (Feb. 2022) 1072–1082, https://doi.org/10.1109/TII.2021.3073685.
[8] Gubanski, S. M., Dernfalk, A., Andersson J, & Hillborg, H. Diagnostic Methods for Outdoor Polymeric Insulators, in IEEE Transactions on Dielectrics and Electrical Insulation, vol. 14, no. 5, 2007.
[9] Wang, S., Lv, F. & Liu, Y. Estimation of discharge magnitude of composite insulator surface corona discharge based on ultraviolet imaging method, IEEE Transactions on Dielectrics and Electrical Insulation, vol. 21, no. 4, 2014.
[10] Z. Zhang, et al., Comparison of different characteristic parameters acquired by UV imager in detecting corona discharge, IEEE Transactions on Dielectrics and Electrical Insulation (2016).
[11] Y, Liu, et al. "Influence of Pollution Degree and Humidity on Surface Discharge Characteristics of Insulators, 2021 3rd Asia Energy and Electrical Engineering Symposium (AEEES)", pp. 175-178. 2021.
[12] L. Jin, J. Ai, Z. Tian, Y. Zhang, Detection of polluted insulators using the information fusion of multispectral images, IEEE Transactions on Dielectrics and Electrical Insulation 24 (6) (Dec. 2017) 3530–3538.
[13] M. Li, Y. Jing, L. Zhang, X. Li, G. Huang and Z. Wang, "Insulator Defect Detection Based on Ultraviolet Imaging and Acoustic Emission Signal," 2020 IEEE 3rd Student Conference on Electrical Machines and Systems (SCEMS), Jinan, China, 2020, pp. 472-475.
[14] D. Ma, et al., Classification of partial discharge severities of ceramic insulators based on texture analysis of UV pulses, High Volt. 6 (6) (2021) 986–996, https://doi.org/10.1049/hve2.12081.
[15] S. Wang, M. Zhou and N. Li, "Discharge Ultraviolet Image Characteristics and Insulation State Evaluation of Polluted and Wet Suspension Porcelain Insulator Strings," in IEEE Transactions on Instrumentation and Measurement, doi: 10.1109/TIM.2024.3417545.
[16] Y. Liu, X. Ji, S. Pei, Z. Ma, G. Zhang, Y. Lin, Y. Chen, Research on automatic location and recognition of insulators in substation based on YOLOv3, High Voltage 5 (2020) 62–68, https://doi.org/10.1049/hve.2019.0091.
[17] N. Davari, G. Akbarizadeh, E. Mashhour, Intelligent Diagnosis of Incipient Fault in Power Distribution Lines Based on Corona Detection in UV-Visible Videos, IEEE Transactions on Power Delivery 36 (6) (2021) 3640–3648.
[18] K. Britto, E. Costa, B. Dias, M. Florentino, G. Lira, Development of DIP-based algorithm for extraction of UV video attributes from corona discharges on polymeric insulators, International Journal of Electrical Power and Energy Systems (2021).
[19] G.A. Rodrigues, C.A. Cordeiro, B.V.S. Araujo, E.O. Freire, G.V.R. Xavier, T. V. Ferreira, "Digital Image Processing Applied to the Reduction of Subjectivity on Ultraviolet Imaging Diagnosis of Insulators, IEEE Electrical Insulation Conference (EIC), Quebec City, QC, Canada 2023 (2023) 1–4, https://doi.org/10.1109/EIC55835.2023.10177307.
[20] Talbot, H., & Najman, L. "Mathematical Morphology: From Theory to Applications". Wiley & Sons, Incorporated, John, 2013.
[21] Szeliski, R. "Computer Vision: Algorithms and Applications". 1. ed. Springer, 2010.
[22] Gonzalez, R. C., Woods, R. E. "Digital Image Processing". 4. ed. Pearson, 2018.
[23] J. Redmon, S. Divvala, R. Girshick and A. Farhadi, "You Only Look Once: Unified, Real-Time Object Detection," 2016 IEEE Conference on Computer Vision and Pattern Recognition (CVPR), Las Vegas, NV, USA, 2016, pp. 779-788, doi: 10.1109/CVPR.2016.91.
[24] H. Rezatofighi, N. Tsoi, J. Gwak, A. Sadeghian, I. Reid, S. Savarese, Generalized intersection over union: A metric and a loss for bounding box regression, in: In Proceedings of the IEEE/CVF Conference on Computer Vision and Pattern Recognition, 2019, pp. 658–666.
[25] Ultralights. (2024, September 5). Comprehensive guide to ultralytics yolov5. Ultralytics YOLO Docs. https://docs.ultralytics.com/yolov5/.
[26] Lin, Tsung-Yi et al; "Microsoft coco: Common objects in context". Computer Vision–ECCV 2014: 13th European Conference, Zurich, Switzerland, Set. 6-12, 2014, Proceedings, Part V 13. Springer International Publishing, 2014. p. 740-755.